Macromolecular Materials and Engineering

Macromolecular Materials and Engineering Open Access

www.mame-journal.de

RESEARCH ARTICLE OPEN ACCESS

Solvent-Mediated Self-Assembly and Hydrogen Bonding in Neutral Alginate: A Molecular Dynamics Study

Vasilii Korotenko | Irina Smirnova | Pavel Gurikov

Thermal Separation Processes, TUHH, Hamburg, Germany

Correspondence: Vasilii Korotenko (vasilii.korotenko@tuhh.de) | Pavel Gurikov (pavel.gurikov@tuhh.de)

Received: 23 July 2025 | **Revised:** 18 December 2025 | **Accepted:** 22 December 2025

Keywords: alginate | hydrogen bonding | molecular dynamics | self-assembly | solvent effects

ABSTRACT

Hydrogen bonding plays a pivotal yet often overlooked role in shaping the structure and dynamics of alginate-based materials. In this study, we use molecular dynamics (MD) simulations to investigate how hydration and solvent environment influence the organization of neutral alginate at the molecular and mesoscale levels. Starting from short isolated chains and progressing toward periodic and entangled systems, we systematically vary water content and examine structural responses using radial and minimal distance distribution functions, as well as geometric analysis based on Alpha Shapes. We find that hydration transforms the polymer matrix from compact, rigid bundles into layered and porous nanostructures, with water acting not merely as a plasticizer but as an active mediator of hydrogen bonding. Even small amounts of water accelerate supramolecular aggregation and promote internal flexibility. At higher hydration, polymer–polymer contacts become more diffuse yet remain structurally coherent. A comparison with ethanol reveals solvent-specific effects on porosity and tortuosity, while the functional surface composition remains robust across all conditions, closely reflecting the molecular stoichiometry of the polymer. These results provide a detailed molecular-level understanding of solvent-mediated self-assembly in alginate and offer general design principles for soft, bioinspired materials where hydrogen bonding is the key structural motif.

1 | Introduction

Cation-crosslinked alginate gels are soft, biodegradable, and deceptively simple materials that exhibit remarkably robust mechanical and structural properties [1]. This strength comes mainly from calcium crosslinks that connect polymer chains via carboxyl groups [2], but also from a more subtle force, namely the hydrogen bonding. Though individually weak, hydrogen bonds weave a resilient network that helps alginate maintain its shape under stress and adapt to environmental changes.

The building blocks of Ca^{2+}-crosslinked alginate hydrogels have been extensively studied across various theoretical levels, ranging from quantum chemical analyses of calcium-mediated junction zones [3, 4], to molecular dynamics simulations of individual chains and their aggregates [2, 5], and further to coarse-grained simulations with implicit cations [6]. However, one specific scenario that has received relatively little attention is the formation and behavior of cation-free alginate gels.

The cation-free alginate gels can be prepared by acidifying an aqueous solution of sodium alginate, as discussed in recent work [7] and references therein. Nanoscaled architecture of neutral, ion-free alginate gels in aqueous environments has been scarcely studied, and to the best of our knowledge, their properties in non-aqueous media remain virtually unexplored. Yet, such cation-free gels represent a simpler model system compared to alginate gels crosslinked with calcium or other metal ions. For instance, alginic acid hydrogels are known to undergo significant shrinkage in poor solvents such as ethanol [8–10], making

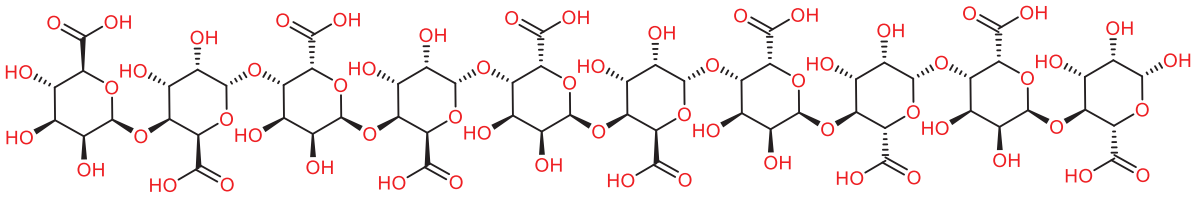

FIGURE 1 | A sequence MGGGGGGMGM with the G/M ratio of 2.34 (70% guluronic acid and 30% mannuronic acid).

them a relevant model system for investigating solvent-induced structural transitions. Neutral alginate, in particular, offers a suitable platform for studying how hydrogen bonding networks and solvent uptake behavior respond to changes in the surrounding environment. Understanding these effects in aqueous and mixed solvent systems provides a foundation for exploring more complex solvent-responsive polymers. Such responsive materials are of growing interest in the development of smart reactors, where solvent composition plays a key role in regulating transport properties and structural organization [11]. This line of research is consistent with recent studies on responsive gels [12] and contributes to a broader effort to design adaptive polymeric systems based on molecular-level insight [13].

In this study, we aim to investigate this protonated, ion-free form of alginate using molecular dynamics (MD) simulations, with a focus on how hydration alone influences hydrogen bonding, conformational mobility, and nanoscale morphology. Given that solvent exchange (particularly from water to an organic solvent such as ethanol) is a key step in converting hydrogels into aerogels [14], we also examine the behavior of alginic acid in ethanol and compare it to that in water. Specifically, in this study, we investigate how hydration influences the lateral aggregation and supramolecular organization of periodic alginate chains, with a particular focus on the role of water molecules in mediating hydrogen bonding between polymer chains and their impact on nanoscale rigidity and flexibility. We further quantify how the solvation level and solvent type (water vs. ethanol) affect the porosity, tortuosity, and internal morphology of alginate networks. Additionally, we examine the intrinsic solvent content retained within the polymer phase and its evolution with increasing hydration in both solvents. Finally, we analyze how hydration alters the surface exposure of functional groups and assess the extent to which surface chemistry reflects the underlying polymer composition.

2 | Methodology

2.1 | Molecular Dynamics

In this study, the molecular composition of alginate was chosen to reflect that of alginate extracted from Laminaria hyperborea, a brown seaweed known for its high guluronic acid content. The selected guluronic-to-mannuronic acid (G/M) ratio of 2.34 corresponds to approximately 70% guluronic acid and 30% mannuronic acid [27, 28]. To represent this composition, a decameric sequence of ten residues, MGGGGGGMGM, was used (Figure 1), along with its extended version consisting of 100 monomers, i.e., $(MGGGGGGMGM)_{10}$. These chains were randomly placed within the simulation box, allowing interactions to form naturally in all directions, thereby enhancing the realism of the model.

Force field parameters were generated using PolyParGen [15] based on the OPLS-AA framework. Cross-interactions were treated using the Lorentz–Berthelot mixing rules, and water was modeled with the TIP3P model. All simulations were carried out using LAMMPS [16]. Temperature was controlled with a Nosé–Hoover thermostat, and pressure regulation employed the Andersen barostat. Long-range electrostatics were treated using the Particle Mesh Ewald (PME) method, with a 15 Å cutoff applied to both Lennard-Jones and Coulomb interactions. Details regarding the use of NPT or NVT ensembles and the corresponding simulation times are provided in the relevant sections.

2.2 | Radial Distribution Function (RDF)

In this study, the RDF is defined as a normalized histogram of distances between atoms A and B, distributed across bins centered at distances r_k (with a total of 100 bins). The RDF describes the probability of finding a pair of atoms separated by a distance within the corresponding interval:

$$\mathrm{RDF}(r_k) = \frac{N_k}{\Delta V\,(r_k) \sum_{i=1}^{n_{bins}} N_i} \tag{1}$$

where N_k is the number of atom pairs with distances falling into the k-th interval, $\Delta V(r)$ is the volume of the spherical shell of thickness Δr corresponding to distance r_k, $\sum_{i=1}^{n_{bins}} N_i$ is the total number of all such atom pairs across all intervals. The volume of a spherical shell is calculated as: $\Delta V(r) = \frac{4}{3}\pi \cdot [(r+\Delta r)^3 - r^3]$, where Δr is the bin width, and r is the lower bound of the interval. The center of each bin, r_k, represents the distance at which the RDF value is averaged for that interval.

Since the RDF is a probabilistic distribution, each value is normalized by the volume of the corresponding spherical shell. This normalization is crucial, as the volume increases with distance, which would otherwise lead to an artificial rise in the number of atom pairs at larger distances. By accounting for the shell volume, the RDF provides an unbiased representation of spatial distribution. For visualization purposes, RDF values can be further scaled so that their total sum across all bins equals 100%. This aids in intuitive comparison but does not reflect the classical physical normalization of the RDF.

2.3 | Minimal Distance Distribution Function (MDDF)

In addition to the RDF, we employed the MDDF as another descriptor. In contrast to the RDF, which accounts for all distances between atom pairs, the MDDF histogram is constructed by considering only the shortest distance between each distinct

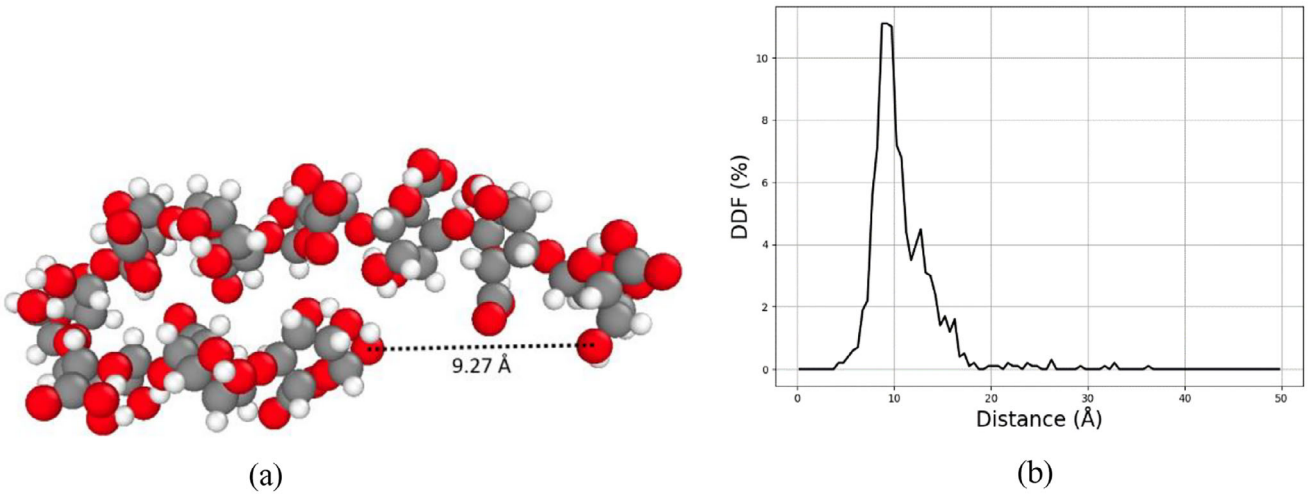

FIGURE 2 | Selected atoms in a single MGGGGGGMGM molecule illustrating (a) the end-to-end distance and (b) the end-to-end distance distribution function (DDF).

pair of atoms. Thus, for every unique pair, only one minimal distance contributes to the distribution. The MDDF is defined as:

$$\mathrm{MDDF}(r_k) = \frac{N_k}{\sum_{i=1}^{n_{bins}} N_i} \quad (2)$$

here, N_k is the number of minimal distances that fall within the k-th bin, and the denominator represents the total number of such minimal distances across all bins. Unlike the RDF, no normalization by the volume of the spherical shell is required, since only one minimal distance per atom pair is counted. This eliminates the need to account for the geometrical increase in volume with distance, making the MDDF a straightforward measure of the spatial distribution of minimal pairwise distances.

3 | Results

3.1 | Short Polymer Chains

First, we investigated the behavior of a set of 27 short molecules with the sequence MGGGGGGMGM in vacuum using MD simulations in the NVT ensemble (constant volume and temperature). This set of molecules tends to cluster into coils rather than forming extended fibrils. When initially arranged in a linear orientation and placed close together, they may transiently align into fiber-like structures, but predominantly form bundles from the medial polymer chain. It is important to note that the simulation was carried out in the gas phase (without water and at extremely low density), which is drastically different from the environment of a real hydrogel.

The molecular end-to-end distance distribution function (DDF, Figure 2) shows a pronounced peak around 10 Å, indicating that the molecules predominantly adopt compact, coiled conformations. The distribution extends up to approximately 40 Å, which corresponds to the fully extended length of the molecule, but shows that such stretched conformations are rare. The observed aggregation behavior is likely driven by the presence of numerous polar groups (—OH, —COOH). In aqueous environments, these groups are expected to interact strongly with surrounding water molecules, screening intermolecular contacts and preventing aggregation. This would promote solubility and favor more extended, linear conformations. Therefore, we anticipate that fibril formation will be more favorable in solution. Based on this, we proceed with further simulations that explicitly include water molecules.

3.2 | Periodic Short Polymer Chains

To prevent short molecules from folding into compact coils and to better analyze lateral interactions, we used a periodic version of the MGGGGGGMGM molecule, where the terminal M units are covalently linked via an ether bond. Rather than forming a physical ring, the chain continues through standard 3D periodic boundary conditions (PBC) along the *X*-axis, effectively creating an infinite polymer. This approach, used in previous studies of polymer self-assembly, minimizes end effects and captures essential lateral interactions using only ten repeating units. In our case, bonding the chain across the box boundary produces the same geometric constraint as the asymmetric periodic boundary conditions (APBC) discussed in refs. [17, 18]. It maintains chain continuity but restricts large-scale bending along the replication axis. This limitation is acceptable here because the focus is on local intermolecular organization and hydrogen bonding, not on global chain conformations. Systems with multiple parallel chains then allow direct observation of lateral aggregation and structural ordering, which are key features of polymer self-assembly.

To achieve realistic densities, the simulation box was first compressed along the *Y* and *Z* directions (perpendicular to the polymer alignment) using an NPT ensemble at 500 K and 100 atm. The system was then relaxed at 300 K and 1 atm, allowing it to return to ambient conditions while maintaining the increased density. A final equilibration run at 300 K and 1 atm for 10 ns ensured full relaxation. To construct a larger system, the resulting box with a single polymer was replicated 3 × 3 times along the Y and Z axes, yielding a 9-chain system.

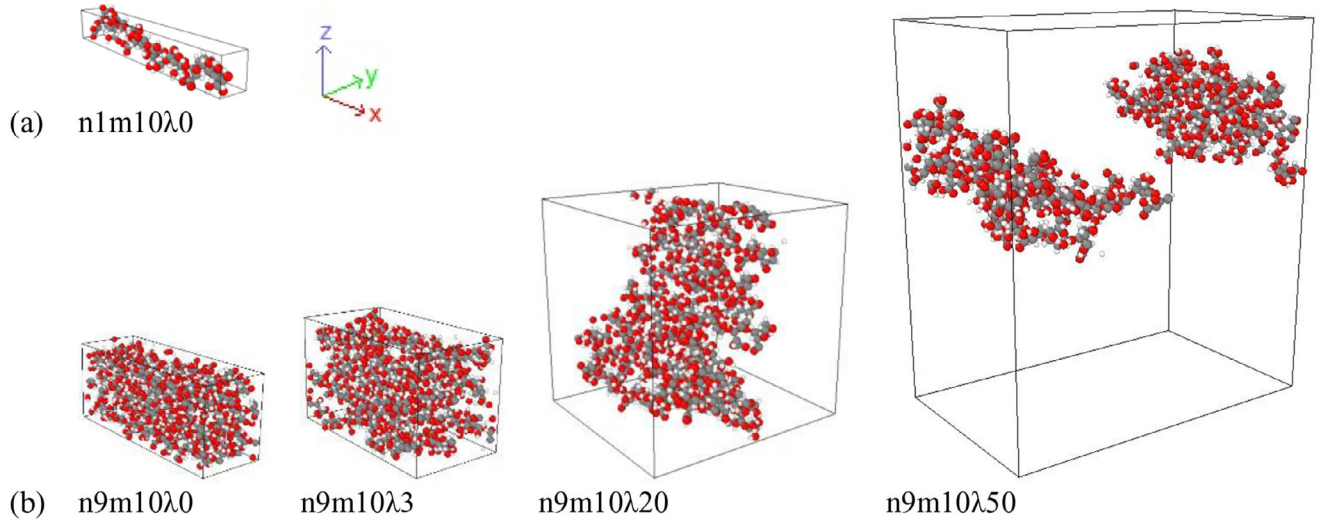

FIGURE 3 | (a) Single periodic (cyclic) chain of the MGGGGGGMGM molecule. (b) Systems containing 9 chains at different hydration levels ($\lambda = 0$, 3, 20, 50), showing how lateral interactions and supramolecular organization of alginate depend on water content. Water molecules are hidden for clarity.

To study hydration effects, we varied the water content, quantified as water uptake (λ), the number of water molecules per monomer. Systems with $\lambda = 0$, 3, 20, and 50 were simulated. Each system is named using the format n9m10λ20, where n is the number of molecules (9), m the number of monomers per chain (10), and λ the hydration level.

To analyze hydrogen bonding and local water structure, we computed RDF. Figure 3 shows the structures formed after 10 ns of simulation, viewed along the y-axis to clearly reveal how the polymer chains are arranged as they pass through the periodic y-walls of the simulation box. This perspective highlights the lateral organization of molecules and their intermolecular interactions. At $\lambda = 3$, water molecules begin to partially infiltrate the space between alginate chains, which may slightly increase the average distance between neighboring molecules. At $\lambda = 20$, the chains remain closely associated and often form connections across the top and bottom boundaries of the simulation box, resulting in elongated, layered arrangements. Here, alginate molecules interact both with one another and with surrounding water, stabilizing a semi-ordered structure. A similar pattern is seen at $\lambda = 50$, where layered morphologies still form, although they are less defined. Rather than cylindrical or rounded aggregates, the system adopts a compromise structure that maximizes both polymer–polymer contacts within the layer and interactions with water.

Figure 4a presents the radial distribution function (RDF) for intermolecular hydrogen bonds, specifically between hydroxyl hydrogen atoms and hydroxyl oxygen atoms of different molecules. At $\lambda = 3$, the RDF reaches a peak of approximately 4.5% at ~10 Å. At $\lambda = 20$ and $\lambda = 50$, the peak remains in the same region but drops to about 3%. Notably, the RDF curves for $\lambda = 20$ and $\lambda = 50$ are nearly identical, suggesting that increasing water content beyond a certain point has minimal effect on the overall distribution of hydrogen bonds between chains. Also shown in Figure 4b is the MDDF, which characterizes the closest intermolecular distances associated with hydrogen bonding. The main MDDF peak occurs around 5 Å, with an occupancy of roughly 20%, indicating a strong tendency for molecules to maintain this close lateral proximity.

Together, the RDF and MDDF analyses provide a fuller picture of intermolecular hydrogen bonding; the RDF describes how likely such interactions are at different distances, while the MDDF highlights preferred nearest-neighbor arrangements. Importantly, the MDDF peak shifts only slightly as water content increases, indicating that the fundamental nature of the interactions remains stable. However, the RDF shows that while alginate–alginate hydrogen bonding persists, higher hydration levels tend to blur the resulting nanostructures, making them more diffuse.

To evaluate the role of water in mediating hydrogen bonding between alginate molecules, we performed additional non-condensed (low-density) simulations (Figure 5). These systems were designed to highlight how hydration affects the formation time of intermolecular aggregates involving all polymer chains in the simulation box. The same modeling protocol as in the main simulations was used, except that the initial compression, annealing, and relaxation steps were omitted. Instead, a simulation box containing a single periodic alginate chain was constructed and replicated 10 × 10 times along the Y and Z axes (Figure 5a). The system was then simulated in the NVT ensemble at 300 K for 2 ns to observe the aggregation behavior under low-density conditions, both in the absence of water ($\lambda = 0$) and in the hydrated state ($\lambda = 3$).

The results show that, due to strong lateral interactions, alginate molecules readily adhere to one another. Once contacts are formed, the chains remain stably associated throughout the simulation, maintaining their relative positions with little to no separation.

When a small amount of water was introduced ($\lambda = 3$) while keeping the system volume constant, alginate molecules still aggregated, but the resulting structures became smoother and more compact, without protruding fragments (Figure 5b). In the formed aggregate, water molecules are located between

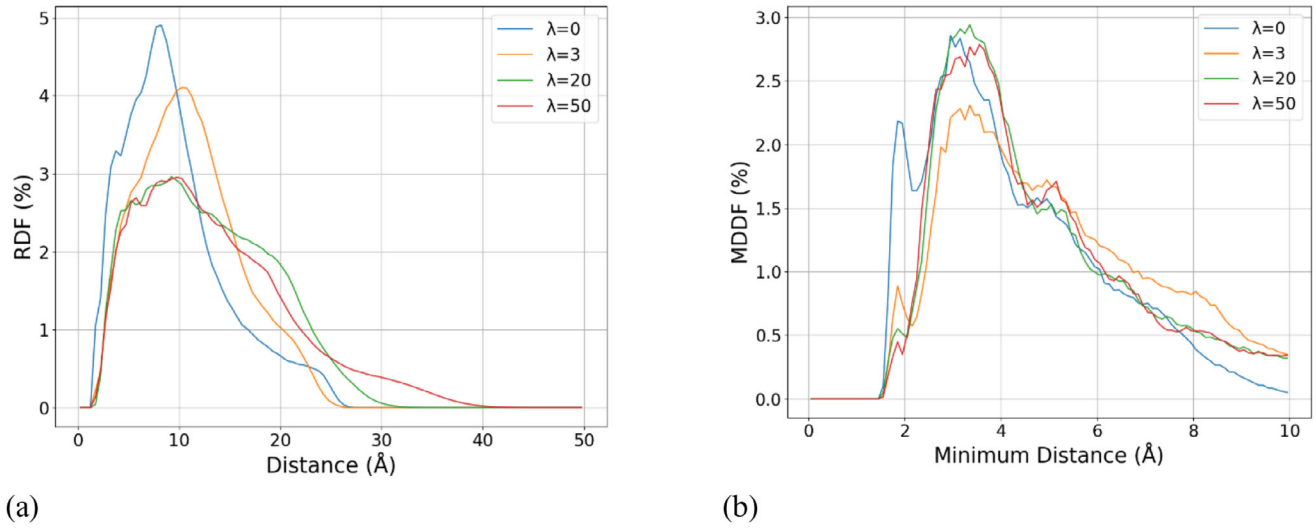

FIGURE 4 | Analysis of all interatomic distances H…O (H_{OH}, H_{COOH}, O_{OH}, O_{COOH}) at different water contents (λ): (a) intermolecular RDF, (b) intermolecular MDDF.

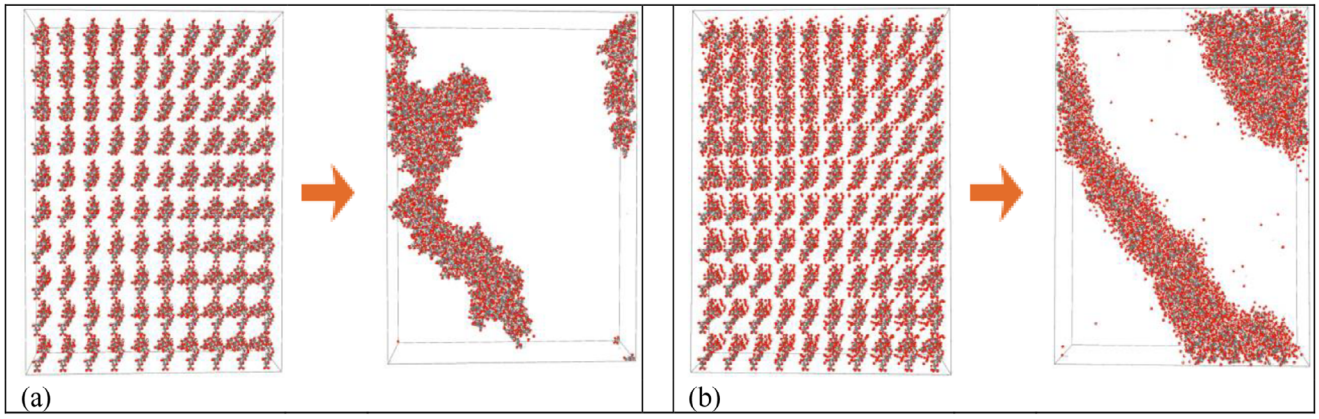

FIGURE 5 | 100 periodically elongated polymers MGGGGGGMGM without (a) and (b) with $\lambda = 3$ (NVT 2 ns T300K). Water molecules are also shown for (b).

the polymer chains, acting as hydrogen-bond bridges. Thus, water plays a key role in mediating interpolymer interactions.

Interestingly, the aggregation behavior of the periodic polymer chains differs under the studied conditions. In the absence of water ($\lambda = 0$), the formation of a large supramolecular structure shown in Figure 5a occurs over approximately 800 ps, as indicated by the RMSD reaching a plateau in Figure 6a, where RMSD is defined as the root mean square displacement of all polymer atoms relative to the initial configuration. In contrast, at $\lambda = 3$ the supramolecular aggregate shown in Figure 5b forms much faster, reaching a stable configuration within about 150 ps (Figure 6b). This difference can be attributed to the presence of water, which mediates polymer–polymer interactions. At the early stages of the simulation, water molecules are already located between the polymer chains and rapidly form hydrogen bonds both among themselves and with the polymer. This network of indirect interactions facilitates chain adhesion and leads to the faster emergence of the nanostructure observed in Figure 5.

Figure 7 compares the RDF for $\lambda = 0$ and $\lambda = 3$. Both show two local maxima. The first, at approximately 4 Å, corresponds to direct hydrogen bonding between hydroxyl groups of different chains. This is confirmed by the MDDF, which shows a sharp peak at the same distance.

As water content increases, both the RDF and MDDF peak intensities at 4 Å decrease, while occupancy at longer distances increases slightly. This suggests that water facilitates a shift from short, strong hydrogen bonds to a more diverse range of longer-distance interactions. The second RDF peak, located around 10 Å, is higher and broader. It reflects the average spacing between polymer chains within the assembled structure and serves as an approximate measure of its internal size.

The 10 Å peak shifts slightly with hydration, indicating that the structure swells as water penetrates and expands the network. Thus, the transition from $\lambda = 0$ to $\lambda = 3$ results in a looser and more structurally adaptive aggregate, characterized by expanded hydrogen-bond connectivity and increased conformational flexibility.

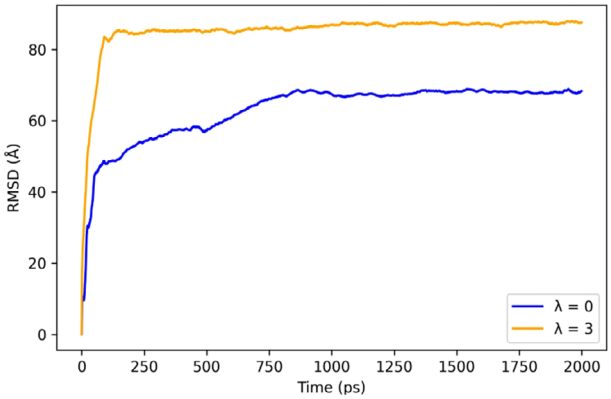

FIGURE 6 | RMSD (Å) as a function of time (ps) for 100 periodically elongated MGGGGGGMGM polymer chains simulated under NVT conditions at 300 K for 2 ns, without solvent mediation ($\lambda = 0$, blue) and with water-mediated interactions ($\lambda = 3$, orange).

3.3 | Longer Polymer Chains

We performed a series of simulations on a system n10m100 containing 10 alginate molecules with the sequence $(MGGGGGGMGM)_{10}$, each consisting of 100 monomers. The fully extended contour length of such a chain is approximately 420 nm (Figure S1). Systems were simulated at various hydration levels (λ = 5, 10, 15, 20, 25, 30, 35, 100). The simulation began with an initial isotropic compression using the NPT ensemble (P = 1000 atm, T = 800 K) to reach a high-density state. This was followed by a gradual relaxation in the NPT ensemble over 0.5 ns, during which the temperature and pressure were reduced from 800 K and 1000 atm to ambient conditions (300 K, 1 atm). To facilitate nanostructure formation and molecular redistribution, we then applied a series of temperature annealing cycles in the NVT ensemble: the temperature was ramped between 300 and 800 K in four consecutive steps, each lasting 0.5 ns, resulting in a total of 2 ns of simulation time. After annealing, the system was equilibrated for 1 ns in the NPT ensemble at 300 K and 1 atm to ensure structural stability. The resulting equilibrated configurations served as starting points for a production run in the microcanonical (NVT) ensemble for 1 ns, during which the RMSD rapidly stabilizes (Figure S2) and reaches a clear plateau. These structures reflect the nature of intermolecular interactions between polymer chains at varying water contents, as well as the formation of primary 3D nanostructural domains.

To evaluate whether hydration affects the internal geometry of the monomer units, we performed a systematic ring puckering analysis based on the Cremer–Pople parameters Q, θ, and φ. Separate θ–φ maps were generated for mannuronic (M) and guluronic (G) residues (Figure S3). For both monomer types, the dominant populations remain centered in the $^4C_1$ region, with only minor excursions toward half-chair and envelope conformations. No systematic shift of the conformational basins is observed as the hydration level λ increases, indicating that ring puckering is essentially insensitive to solvent content in the ion-free system. M residues display slightly broader distributions, consistent with their known higher flexibility, while G residues remain more localized and structurally rigid. Overall, all monomers retain their characteristic chair conformations across the entire λ range, and ring puckering does not contribute to the hydration-dependent structural trends discussed in this work.

To visualize the internal organization of the system, we applied the AlphaShape method [19], which constructs a geometric envelope around discrete atomic coordinates using Delaunay triangulation. This approach outlines the regions occupied by the polymer and reveals the morphology of the surrounding pore architecture. In this work, the AlphaShape surfaces were generated with the sphere radius parameter set to 7 Å, which provides an optimal balance between surface smoothness and structural detail. Smaller values tend to over-segment the surface, while larger ones may oversmooth fine features. Figure 8 presents the system with water molecules hidden, allowing a clearer view of the polymer chains. This representation demonstrates nanophase separation between a polymer-rich phase and a water-rich phase. AlphaShape surfaces constructed using only polymer atoms highlight the spatial organization of the polymer domains and the nanopores that correspond to regions originally filled with water. As the hydration level (λ) increases, the simulation box expands from about 7 nm at λ = 5 to roughly 11.5 nm at λ = 35, reflecting the higher solvent content and the increased computational cost associated with larger systems. Accordingly, the total volume of the system increases almost linearly with increasing λ, whereas the volume of the polymer phase remains nearly constant, indicating that hydration primarily expands the pore space rather than the polymer nanophase itself (Figure 9).

The pore size obtained from the AlphaShape analysis (approximately 5 nm) is consistent with the experimentally observed nanoporous structure of ionically crosslinked alginate gels (typical pore size around 5 nm [20, 21]), indicating that the simulated morphologies reproduce realistic nanoscale features of dense ionic alginate nanophases. However, we note that the present simulations focus on protonated alginate. Small-angle X-ray scattering (SAXS) data show that protonated alginate forms much thicker fibrillar domains with a characteristic radius of about 15 nm, which is significantly larger than the linear dimensions of our simulation box and therefore cannot be captured within the current computational setup [22].

To assess whether the explicit treatment of water influences the morphology of the polymer nanophase, we performed a control simulation for the λ = 35 system using an implicit solvent model with a dielectric constant of 78.5. The final NVT configuration from the explicit-solvent trajectory was taken from its last frame, all water molecules were removed, and this structure was then used as the starting point for a continued NVT simulation in the implicit environment. The resulting configuration remains structurally similar to the explicit solvent reference and rapidly converges to a stable RMSD plateau (Figure S4). The volume of the polymer nanophase changed only minimally, from 209 nm^3 in the explicit system to 212 nm^3 in the implicit one (Figure S5). This very small difference indicates that the overall compactness and density of the polymer network are essentially preserved even without explicit water. These observations suggest that an implicit solvent model can reproduce the global geometry of the nanophase with good fidelity and may significantly reduce computational cost for neutral polysaccharides. However, implicit solvation cannot describe water-mediated effects that are central to this study, including hydrogen-bond bridges between chains

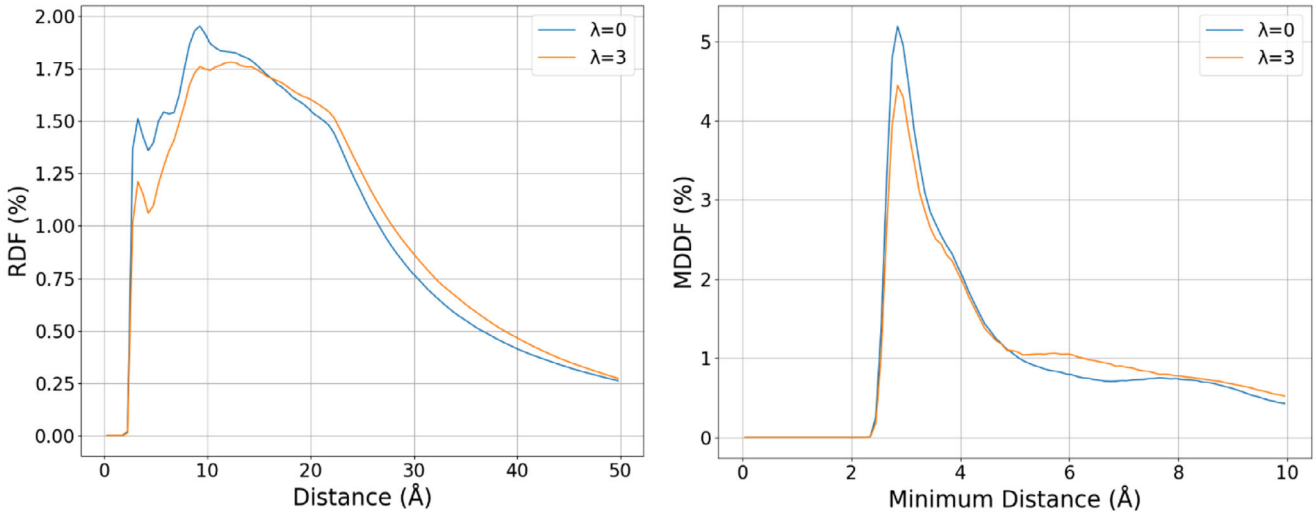

FIGURE 7 | Analysis of intermolecular hydrogen bonds using RDF and MDDF at different water contents (λ).

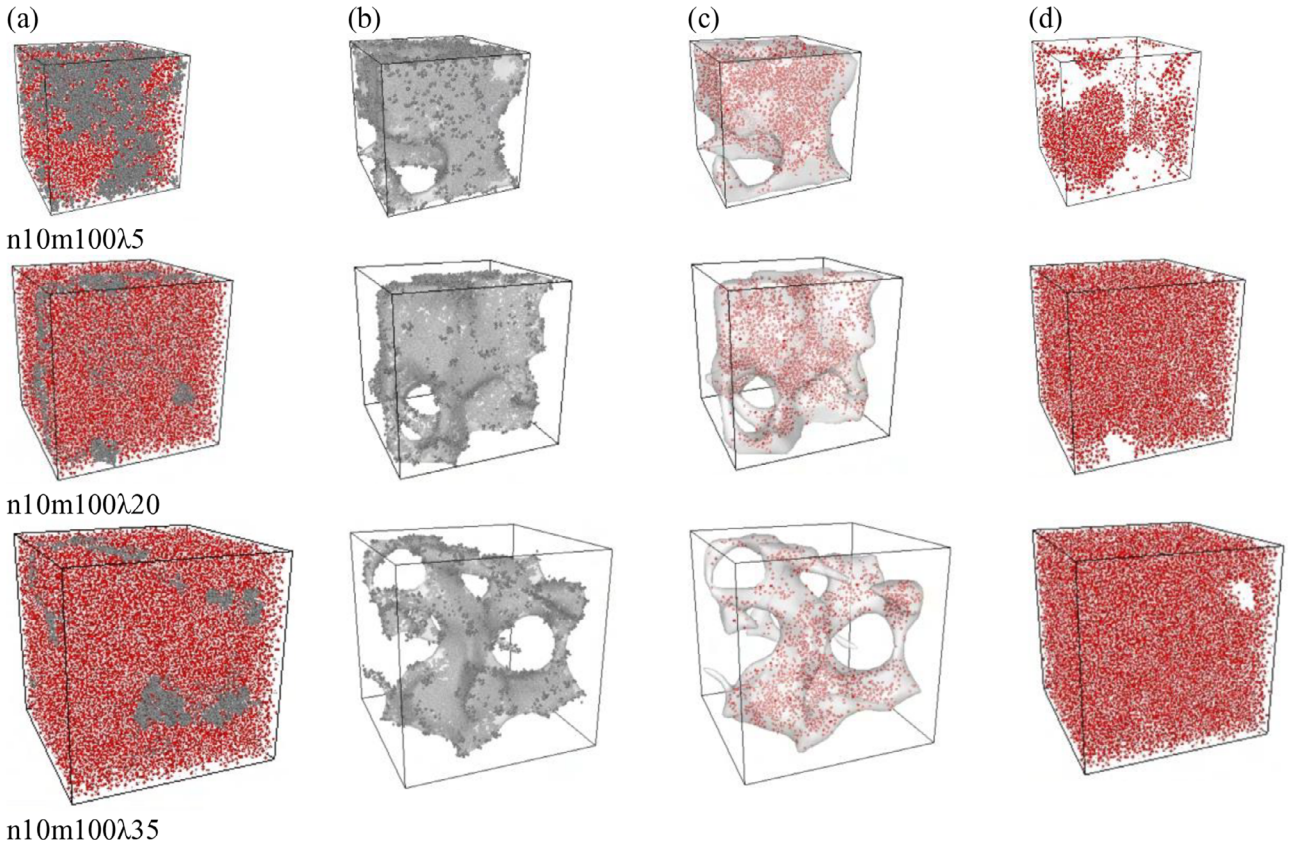

FIGURE 8 | Resulting polymer nanostructures of alginate at different hydration levels ($\lambda = 5, 20, 35$). (a) Complete system including both polymer and water molecules. (b) Polymer atoms only, colored in gray, enclosed by the AlphaShape surface representing the polymer nanophase. (c) Same AlphaShape surface, now showing the intrinsic water molecules located inside the polymer nanophase. (d) External (pore) water remaining outside the polymer nanophase.

and the penetration of water into local nanocavities. For this reason, all production simulations reported here were carried out with explicit water.

AlphaShape surfaces not only visualize polymeric nanostructures but also provide a basis for quantitative analysis. Using these surfaces, we evaluated key structural characteristics of the 3D simulation box, namely tortuosity and porosity. Tortuosity (τ) is defined as the ratio of the actual transport path length through the pore space to the straight-line distance between two points (Figure 10). Porosity (ε) is defined as the fraction of accessible pore volume relative to the total volume of the system. Both

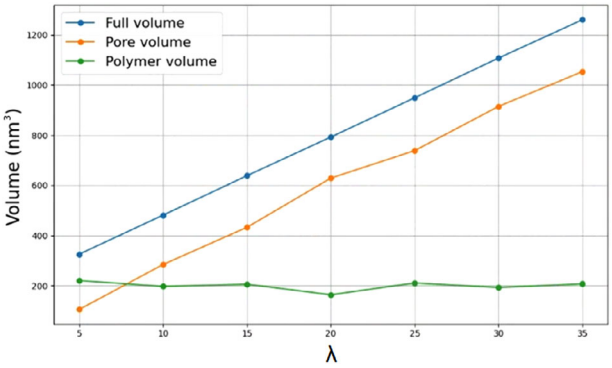

FIGURE 9 | Total, pore, and polymer volumes as functions of hydration level λ.

parameters were calculated from AlphaShape-derived 3D masks using voxel-based shortest-path and volume-fraction algorithms implemented in PoreSpy [23], which directly compute these quantities.

In addition to water, ethanol is commonly used in the processing and post-treatment of alginate-based materials, for example, in gel dehydration and controlled precipitation [24, 25]. Although alginate does not dissolve in pure ethanol, the distinct properties of ethanol, including its lower polarity, larger molecular volume, and weaker hydrogen bonding compared to water, make it a useful reference solvent for studying polymer–solvent interactions. By comparing alginate behavior in both solvents, we examine how solvent characteristics influence the formation, dynamics, and internal structure of biopolymer networks.

Increasing the hydration level (λ) leads to a more porous structure. In water, porosity rises from about 0.4 to 0.9, while in ethanol it ranges from 0.75 to 0.97. This higher porosity in ethanol-based systems likely results from the larger molecular volume of ethanol compared to water at the same λ. In parallel, the tortuosity of the pore network decreases with increasing λ, reflecting a transition toward more linear and accessible pathways. In water, tortuosity drops from approximately 1.4 to 1.15, and in ethanol from about 1.27 to 1.06. These lower values indicate improved permeability and a more open structure, especially in ethanol, where the larger solvent molecules promote wider, less convoluted nanopores.

When the same analysis is applied to the polymeric nanophase, a contrasting trend is observed. As λ increases, the tortuosity of the polymer network rises slightly, in contrast to the decreasing tortuosity seen in the pore phase. However, the difference between water and ethanol is minimal. In water, polymer tortuosity increases from approximately 1.2 to 1.6, and in ethanol from 1.4 to 1.6. This suggests that the internal geometry of the polymer remains similarly complex in both solvents, with the solvent type having little influence on the intrinsic winding of the polymer structure.

Next, we analyzed all interatomic distances between hydrogen and oxygen atoms within hydroxyl (—OH) and carboxyl (—COOH) groups. In other words, we considered all possible H…O pairs formed by atoms belonging to these functional groups, distinguishing between intramolecular and intermolecular interactions. The distance distributions shown in Figure 11 are averaged over all frames, and an inspection of individual snapshots reveals no substantial frame-to-frame variations over the course of the simulation (Figure S6).

In the MDDF (Figure 11b) for intramolecular H…O distances, the first peak appears at around 1.2 Å, which likely corresponds to hydrogen bonds (H ··O) within a single monomer. A second peak is observed near 3 Å, presumably reflecting interactions between different monomers, not necessarily adjacent ones. Since the polymer often adopts a coiled conformation, hydrogen bonds can form across non-neighboring units, as long as the relevant groups come into spatial proximity.

Surprisingly, the distributions of intramolecular H…O distances, both in the RDF and MDDF, remain virtually unchanged as λ increases. The shape and position of the peaks stay consistent, indicating that the internal structure of the molecules is largely unaffected by the hydration level.

As the value of λ increases, the intensity of the peak at 4.5 Å in the MDDF gradually decreases, while the overall distribution becomes broader and extends toward longer distances. In other words, the probability shifts from well-defined short-range contacts to a wider range of more distant interactions. This suggests that with increasing water content, the polymer structure becomes less compact, and the hydrogen bonding between chains becomes more diffuse and mediated, often involving bridging water molecules.

Is it possible that some water molecules reside within the polymer nanophase itself, embedded in its nanostructure and thereby increasing the average intermolecular H···O distances between functional groups? To explore this, we tracked the positions of all water molecules across simulation frames and classified them based on whether they were located inside or outside the polymer nanophase. The distinction was made by checking if a molecule was enclosed within the AlphaShape-defined polymer volume or positioned in the surrounding solvent region. This analysis enabled us to compute $\lambda_{\text{intrinsic}}$, defined as the number of solvent molecules per monomer located within the polymer nanophase. We then examined how $\lambda_{\text{intrinsic}}$ changes with total λ.

Figure 12 shows that $\lambda_{\text{intrinsic}}$ is consistently higher for water than for ethanol. This is likely due to the smaller size of water molecules and their ability to donate two hydrogen bonds of O—H··O type, which can facilitate stronger interactions with the polymer. These properties make it easier for water to penetrate and distribute throughout the polymer nanophase, especially at low hydration levels.

For both solvents, $\lambda_{\text{intrinsic}}$ decreases as total λ increases. This trend reflects a conformational expansion of the polymer, which reduces the number of small internal pockets capable of retaining solvent molecules. At higher hydration levels, visual inspection reveals a greater number of isolated polymer fragments that no longer interact with neighboring chains or even with themselves. This reduces the likelihood of forming nanoscopic cavities that could trap solvent. The presence of excess water between polymer segments likely prevents their aggregation within the accessible timescale and computational limits of our simulations. As the

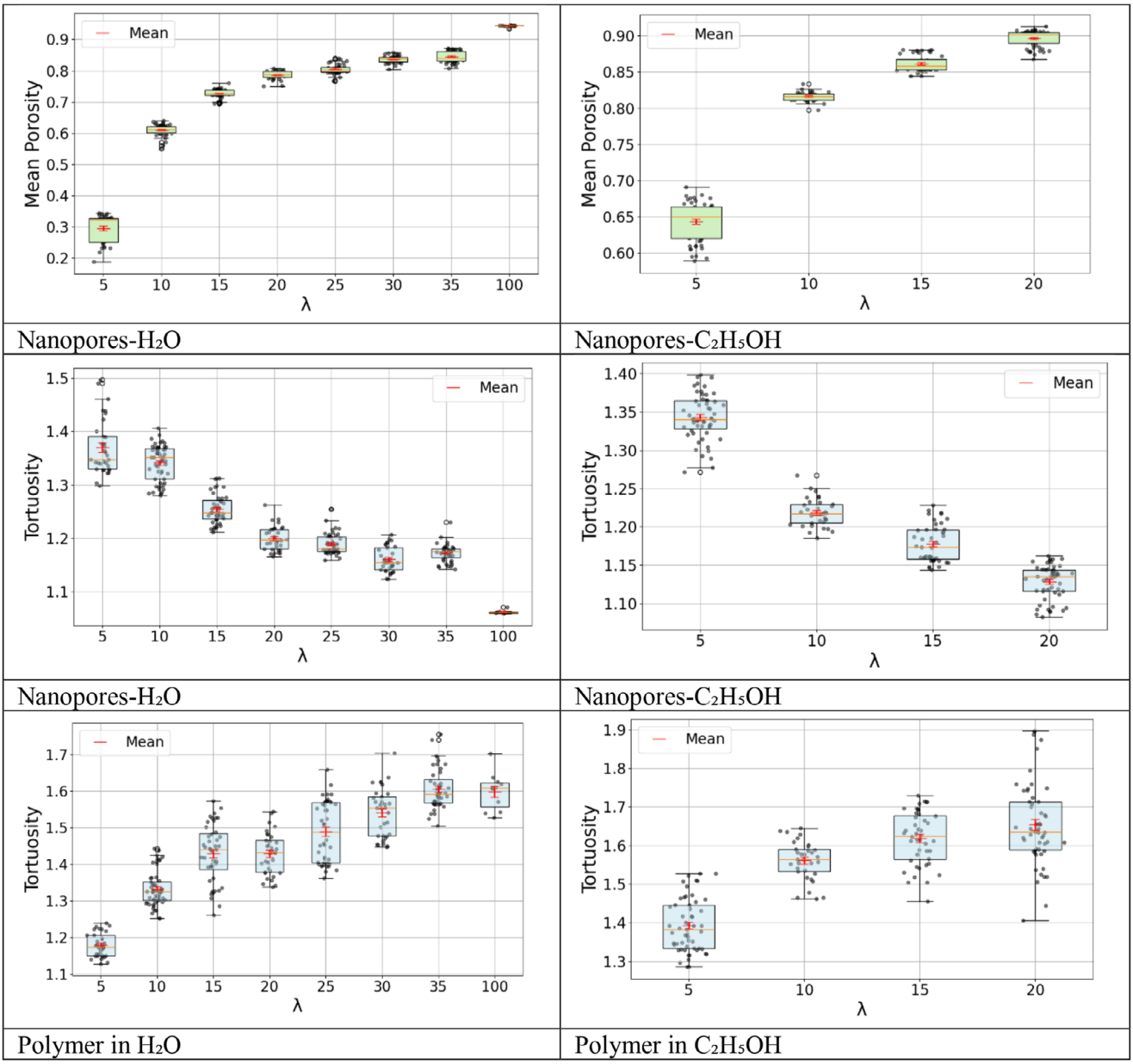

FIGURE 10 | Structural parameters calculated using the AlphaShape method as a function of hydration level (λ). Top row: porosity. Middle row: tortuosity of the pore network. Bottom row: tortuosity of the polymer phase. Left column: systems hydrated with H_2O. Right column: systems hydrated with C_2H_5OH. Each boxplot shows the distribution of values across simulation frames and replicates, with red bars indicating the mean and standard error.

structure becomes more open, confined regions become less frequent, resulting in a lower internal solvent concentration.

We also quantified the individual contributions of the total, pore, and polymer volumes to examine how the overall morphology evolves with hydration (Figure 9). The results show that both the total and pore volumes increase almost linearly with λ, reflecting the higher solvent content, whereas the absolute volume of the polymer nanophase remains nearly constant within statistical uncertainty (~5%). This indicates that hydration primarily expands the water-filled pores rather than changing the intrinsic density of the polymer phase. Consequently, the retention of water is governed not by the total polymer amount but by the local packing of chains capable of forming enclosed nanostructures. Such ordered regions create confined environments where water molecules can be trapped within the polymer nanophase. Therefore, $\lambda_{intrinsic}$ is determined by the ability of the chains to assemble into configurations that provide suitable pockets for solvent retention.

The survival curve (Figure 13a) and the residence time histogram (Figure 13b) provide complementary views of the dynamics of intrinsic water molecules confined within the polymer network. Both analyses are based on a fixed cohort of water molecules identified within the final 100 simulation frames, where the geometry of the polymer nanophase has already reached structural relaxation. Each frame corresponds to 1 ps, allowing a direct observation of molecular survival over a 100 ps time window.

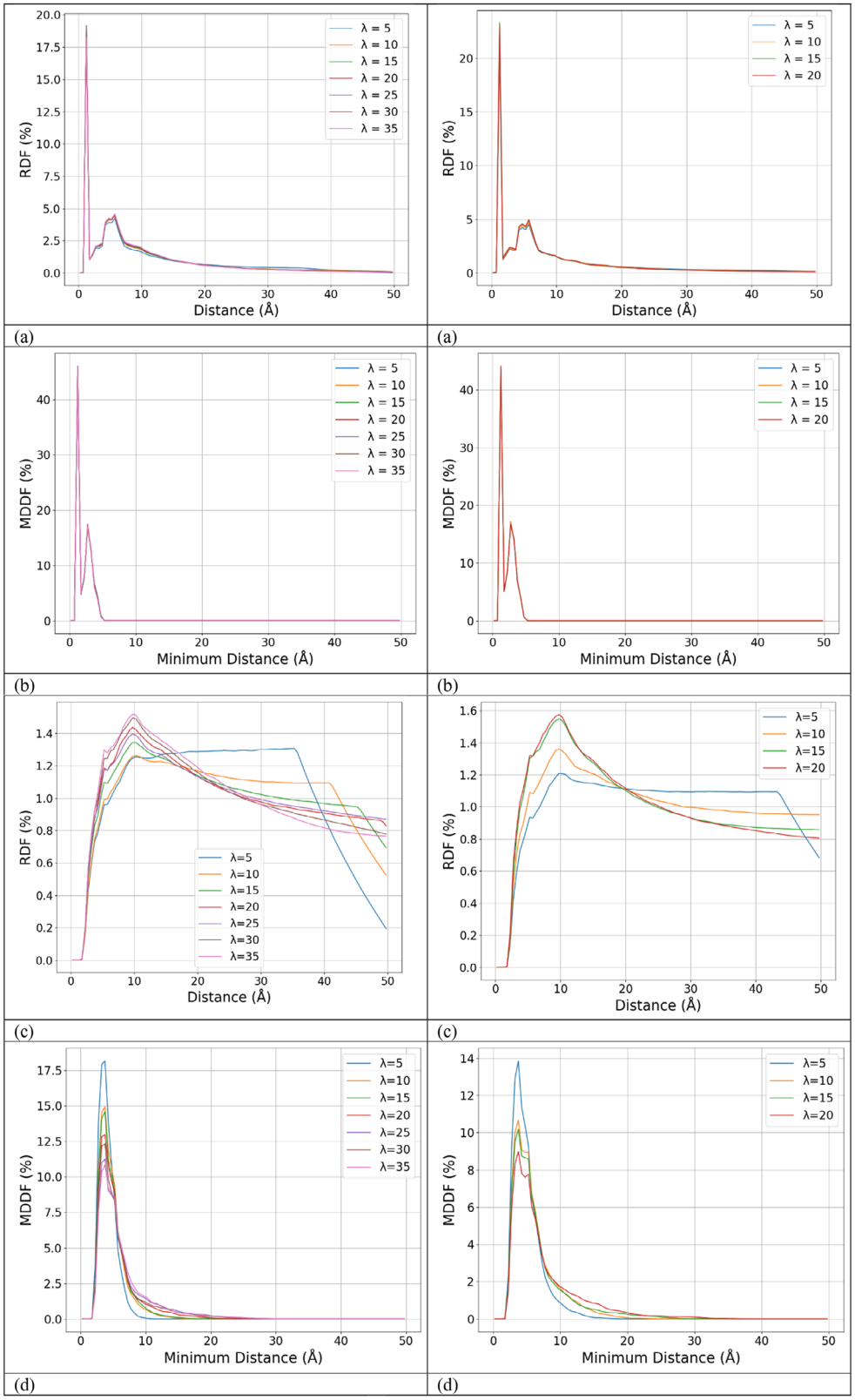

FIGURE 11 | Analysis of all interatomic distances H…O (H_{OH}, H_{COOH}, O_{OH}, O_{COOH}) at different solvent contents (λ) in water (left) and ethanol (right): (a) intramolecular RDF, (b) intramolecular MDDF, (c) intermolecular RDF, (d) intermolecular MDDF.

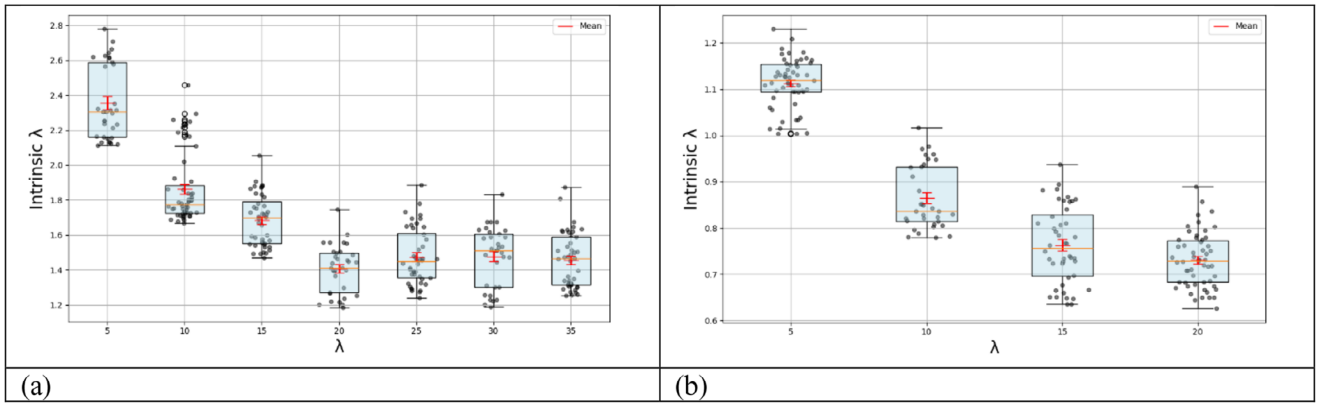

FIGURE 12 | Intrinsic solvent content within the polymer nanophase, defined as the number of solvent molecules per monomer located inside the AlphaShape-defined polymer volume. (a) Systems hydrated with H_2O. (b) Systems hydrated with C_2H_5OH. Each boxplot shows distributions across simulation frames and replicates, with red bars indicating the mean and standard error.

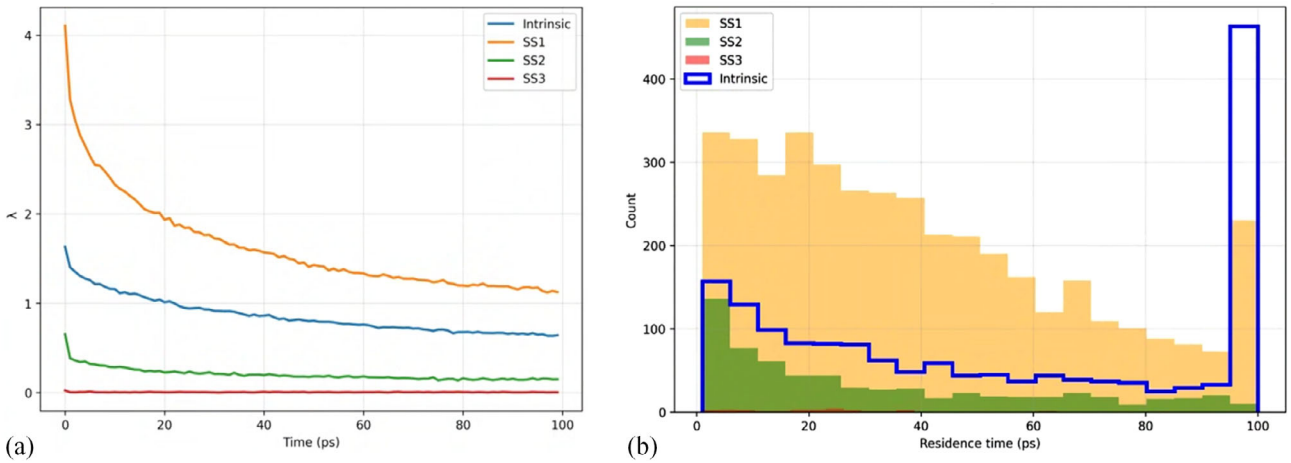

FIGURE 13 | Survival curve (a) and residence (b) time distribution of intrinsic water within the polymer nanophase, based on a fixed cohort identified within the final 100 ps of simulation.

The cohort is defined as the set of water molecules located inside the intrinsic surface at the initial frame of this window, after which only these molecules are tracked. The survival curve (Figure 13a) shows a sharp initial drop corresponding to the rapid loss of interfacial members of this cohort, which leave the polymer domain due to diffusive motion or minor breathing fluctuations of the polymer surface. After this initial relaxation, the remaining cohort members are mainly located within the inner nanophase of the gel and display nearly stationary behavior, indicating a strong suppression of exchange with the external solvent.

The residence time distribution (Figure 13b) presents this temporal behavior in statistical form. It exhibits a characteristic bimodal shape: a sharp maximum at short residence times followed by a broad plateau and a secondary rise at longer times (≥100 ps). This shape reflects the coexistence of two distinct water populations, a rapidly exchanging interfacial fraction and a slowly relaxing, deeply trapped fraction.

In physical terms, the two regimes, the fast exponential-like decay at short times and the quasi-stationary plateau at longer times, represent the transition from weakly bound surface water to strongly confined core water. Such behavior is consistent with survival functions reported for water in nanoporous materials, proteins, and polymer gels, where dynamical heterogeneity arises from spatially varying confinement and hydrogen-bond network topology.

Our analysis of the survival dynamics and residence time distribution further demonstrates a clear separation between rapidly exchanging interfacial molecules and a slowly relaxing, long-lived population localized within the polymer nanophase. This dual-regime behavior agrees with the "core–shell" model proposed by authors [26] for water in alginate gels, where the first hydration layer, located about 0.4 nm from the polymer surface, exhibits restricted mobility and structural perturbation, while the core water retains near-bulk diffusivity and orientational order. In both cases, the interfacial fraction undergoes a rapid exponential-like decay in residence probability, followed by a quasi-stationary plateau corresponding to strongly confined water. However, our cohort-based approach complements their results by directly capturing the gradual loss of intrinsic water molecules through diffusive escape across the fluctuating polymer boundary. Thus,

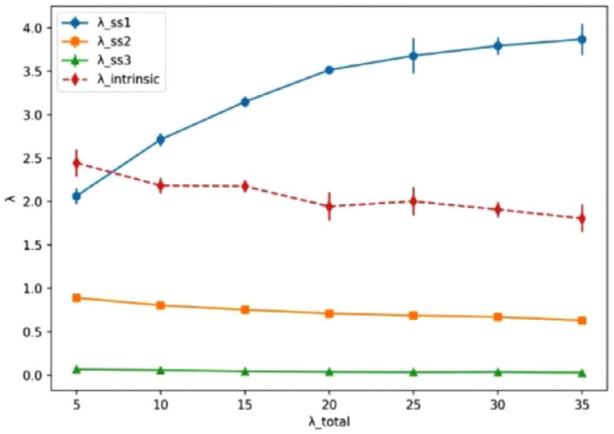

FIGURE 14 | Dependence of λ_{ss1}, λ_{ss2}, λ_{ss3}, and $\lambda_{intrinsic}$ on the total hydration level λ. Here, λ_{ss1}, λ_{ss2}, and λ_{ss3} correspond to the number of water molecules contacting one, two, or three alginate chains, respectively (normalized per 1000 monomers), while $\lambda_{intrinsic}$ represents the number of water molecules located inside the polymer nanophase. The results show that λ_{ss1} increases with hydration, λ_{ss2} remains small but persistent, and $\lambda_{intrinsic}$ decreases, indicating a gradual redistribution of water from confined to interchain regions.

the survival analysis confirms and extends the core–shell picture by linking static structural confinement with explicit temporal dynamics of molecular exchange.

We also quantified the bridging character of solvent molecules by tracking how many polymer chains each water molecule contacts. A water molecule was assigned to solvation shell one (ss_1), two (ss_2), or three (ss_3) if its oxygen atom was located within 3.5 Å of H or O atoms belonging to one, two, or three different chains, and the corresponding populations were denoted as λ_{ss1}, λ_{ss2}, and λ_{ss3}. These quantities are shown in Figure 13 alongside $\lambda_{intrinsic}$ and provide complementary structural information. The λ_{ss1} population increases with hydration and represents water molecules that interact with the polymer without forming true bridges. In contrast, λ_{ss2}, although small in magnitude, persists across all hydration levels and corresponds to genuine two-chain bridges that mediate polymer-polymer contacts. The λ_{ss3} population remains very minor, as three chain contacts are geometrically rare. Together with $\lambda_{intrinsic}$, which reflects water retained inside the polymer nanophase, these quantities characterize the balance between interfacial, bridging, and deeply confined water in the system.

As shown by the λ_{ss1}, λ_{ss2}, λ_{ss3}, and $\lambda_{intrinsic}$ profiles, hydration produces a systematic redistribution of water between different structural environments of the polymer network (Figure 14). The λss_1 population, representing water molecules that interact with a single chain, increases steadily with λ, consistent with enhanced surface wetting at higher hydration. In contrast, λ_{ss2} remains small but persistent across all systems, indicating that true two-chain bridges are rare but constitute a stable structural motif independent of λ. Three-chain contacts (λ_{ss3}) are negligible, reflecting the low probability of simultaneous proximity to three chains. At the same time, $\lambda_{intrinsic}$ decreases monotonically with λ, demonstrating that the nanocavities capable of trapping water become less prevalent as the polymer network expands and loses its most confined regions. Together, these trends reveal a shift from deeply confined water to predominantly interfacial and weakly bridging environments as hydration increases.

Looking at Figure 8, one naturally wonders: what is the actual surface composition of these hydrated nanostructures? Oxygen atoms are consistently observed at the interface, but to which functional groups do they belong? Since hydration reshapes the internal organization and weakens intermolecular contacts, it may also affect which chemical groups become exposed at the surface.

To investigate this, we calculated the minimum distances from the polymer surface (defined using the AlphaShape method) to all oxygen atoms in hydroxyl groups and carbon atoms in carboxyl groups. A group was classified as surface-exposed if at least one of its key atoms was located within 2.0 Å of the surface. This allowed us to identify and count exposed groups across different hydration states (Figure 15).

Our model polymer $(MGGGGGGMGM)_{10}$ contains 100 carboxyl and 202 hydroxyl groups, corresponding to a molar fraction of $x_{OH} = 0.67$ and $x_{COOH} = 0.33$. These values were used as a reference to compare against the surface composition observed in simulations.

Figure 15a,b shows how the number of surface-accessible atoms changes with hydration level λ. Each data point represents a configuration sampled every 10 frames from five independent simulations, and red bars indicate the mean with standard error. The results show that both hydroxyl and carboxyl groups become increasingly surface-exposed as λ increases, with hydroxyl groups showing the most pronounced growth between $\lambda = 15$ and 25, followed by a slight decline at higher hydration levels. This suggests that moderate hydration promotes functional group exposure, while excessive swelling may lead to partial burial of groups within the polymer network.

Interestingly, the data points for each λ often cluster into two or three narrow bands, reflecting the natural variability introduced by different initial polymer arrangements in each replica. This underlines the importance of performing multiple independent simulations when analyzing structurally disordered systems.

Figure 15c shows the O_{OH}/C_{COOH} surface ratio, which generally stays within ~2.0 to 2.5, consistent with the polymer's intrinsic stoichiometry. A notable peak at $\lambda = 25$ indicates transient surface enrichment in hydroxyl groups. This is further summarized in Figure 15d, where solid lines represent the mean number of each group on the surface, and the dashed line tracks their ratio. Again, the most prominent shift occurs at $\lambda = 25$.

Overall, the surface composition closely mirrors the underlying chemical structure of the polymer. Although hydration causes moderate shifts, particularly at intermediate λ, the O_{OH}/ C_{COOH} ratio remains largely consistent with the molecular formula. This suggests that for neutral alginate, the surface group distribution can be reliably predicted from the polymer's chemical formula, a valuable property for rational materials design.

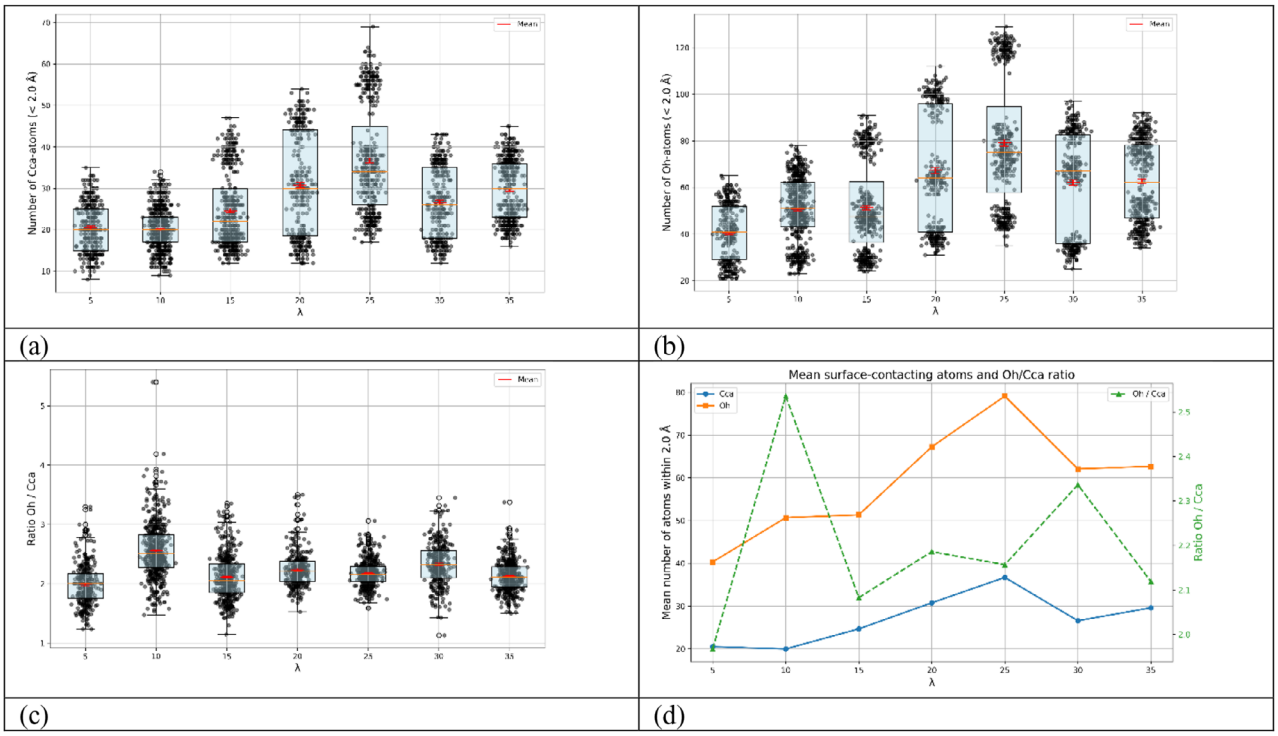

FIGURE 15 | Distribution of C_{COOH} (carboxy) and O_{OH} (hydroxy) atoms located within 2.0 Å of the surface as a function of water content λ. (a) and (b): boxplots of the number of C_{COOH} and O_{OH} atoms, respectively. Each box represents the median, interquartile range, and outliers across all configurations (every 10th frame and 5 simulation replicates). Red bars indicate the mean values with standard error bars. (c): distribution of the O_{OH} / C_{COOH} ratio using the same statistical representation. (d): average number of C_{COOH} and O_{OH} atoms as a function of λ, with the O_{OH} / C_{COOH} ratio shown on a secondary axis (dashed line).

4 | Conclusions

Our work demonstrated that hydration is more than a background condition; it acts as an active sculptor of structure in neutral alginate. Our simulations reveal that water not only screens electrostatic interactions but also transforms the internal morphology of the polymer matrix. At low hydration, hydrogen bonding promotes the formation of compact and rigid assemblies. As water content increases, these structures swell and soften, giving rise to porous and interconnected networks stabilized by a dynamic balance of polymer–polymer and polymer-solvent interactions.

We show that even small amounts of water accelerate supramolecular aggregation by mediating transient hydrogen bonds. Water acts not as a passive diluent but as a cooperative linker. At higher hydration levels, hydrogen bonding becomes more diffuse and often mediated by solvent molecules, which promotes morphological flexibility without compromising structural coherence. Ethanol induces similar effects and forms slightly more convoluted nanostructures at low solvation levels, highlighting how solvent properties influence nanoscale organization.

Geometric analyses based on Alpha Shapes reveal a consistent trend. Hydration reduces tortuosity and enhances porosity in solvent-accessible channels, while the polymer phase itself becomes more flexible and structurally intricate. Remarkably, the surface distribution of hydroxyl and carboxyl groups remains close to the intrinsic stoichiometry of the polymer across hydration levels. This chemical robustness suggests that surface functionality in such soft materials can be predicted directly from molecular composition, which is a valuable principle for rational material design.

In summary, water does not merely wet the polymer. It reshapes the entire hydrogen-bonding landscape, modulates internal dynamics, and defines the mesoscale architecture. Understanding this transformation is essential for mastering the self-assembly of alginate and related biomaterials. As in many soft matter systems, structure defines function, and water, always the quiet architect, remains the key to unlocking it.

Acknowledgements

We would like to express our gratitude to the Deutsche Forschungsgemeinschaft (DFG, German Research Foundation) for funding this project through the SFB 1615 (503850735). V.K. expresses gratitude for the computational resources provided by the Max Planck Computing and Data Facility (MPCDF). Publishing fees are supported by the Funding Programme Open Access Publishing of Hamburg University of Technology (TUHH). LAMMPS input files are published on TUHH TORE https://doi.org/10.15480/882.15182.

Conflicts of Interest

The authors declare no conflicts of interest.

Data Availability Statement

The data that support the findings of this study are openly available in LAMMPS Simulation Files Supporting the Study “Molecular Dynamics

Study of Hydrogen Bonding in Neutral Alginate: Structural Insights and Solvent Uptake Effects" at https://doi.org/10.15480/882.15182, reference number 1142055618.

References

1. C. A. García-González, M. Alnaief, and I. Smirnova, "Polysaccharide-Based Aerogels—Promising Biodegradable Carriers for Drug Delivery Systems," *Carbohydrate Polymers* 86, no. 4 (2011): 1425–1438.

2. H. Hecht and S. Srebnik, "Structural Characterization of Sodium Alginate and Calcium Alginate," *Biomacromolecules* 17, no. 6 (2016): 2160–2167.

3. W. Plazinski and M. Drach, "Calcium-α-l-Guluronate Complexes: Ca^{2+} Binding Modes from DFT-MD Simulations," *The Journal of Physical Chemistry B* 117, no. 40 (2013): 12105–12112.

4. W. Plazinski and M. Drach, "Binding of Bivalent Metal Cations by α-l-Guluronate: Insights from the DFT-MD Simulations," *New Journal of Chemistry* 39, no. 5 (2015): 3987–3994.

5. M. B. Stewart, S. R. Gray, T. Vasiljevic, and J. D. Orbell, "Exploring the Molecular Basis for the Metal-Mediated Assembly of Alginate Gels," *Carbohydrate Polymers* 102 (2014): 246–253.

6. P. N. Depta, P. Gurikov, B. Schroeter, et al., "DEM-Based Approach for the Modeling of Gelation and its Application to Alginate," *Journal of Chemical Information and Modeling* 62, no. 1 (2021): 49–70.

7. N. Leventis, R. Soni, J. Bartels, and R. Begag, "Form-Factor Control of Alginate Aerogels via Thixotropic Sols: From Monoliths to Fibers to Films," *ACS Applied Materials & Interfaces* 17 (2025): 9891–9912.

8. F. Ferrero, P. Campagna, and N. PICCrNINI, "Shrinking Kinetics of Calcium Alginate Beads in Alcoholic Soda," *Chemical Engineering Communications* 15, no. 1–4 (1982): 197–206.

9. Q. Zhou, C.-P. Chng, Y. Zhao, et al., "Ethanol-Induced Gelation Enables Direct Three-Dimensional Printing of Sodium Alginate Hydrogel," *Materials & Design* 239 (2024): 112746.

10. P. Gurikov, S. Raman, D. Weinrich, M. Fricke, and I. Smirnova, "A Novel Approach to Alginate Aerogels: Carbon Dioxide Induced Gelation," *RSC Advances* 5, no. 11 (2015): 7812–7818.

11. X. Hu, J. Karnetzke, M. Fassbender, et al., "Smart Reactors—Combining Stimuli-Responsive Hydrogels and 3D Printing," *Chemical Engineering Journal* 387 (2020): 123413.

12. X. Hu, C. Spille, M. Schlüter, and I. Smirnova, "Smart Structures—Additive Manufacturing of Stimuli-Responsive Hydrogels for Adaptive Packings," *Industrial & Engineering Chemistry Research* 59, no. 43 (2020): 19458–19464.

13. K. M. Eckert, J. Bonsen, A. Hajnal, et al., "Enhancing Swelling Kinetics of pNIPAM Lyogels: The Role of Crosslinking, Copolymerization, and Solvent," *Fluid Phase Equilibria* 597 (2025): 114462.

14. P. Gurikov and I. Smirnova, "Non-Conventional Methods for Gelation of Alginate," *Gels* 4, no. 1 (2018): 14.

15. M. YABE, K. MORI, K. UEDA, and M. TAKEDA, "Development of PolyParGen Software to Facilitate the Determination of Molecular Dynamics Simulation Parameters for Polymers," *Journal of Computer Chemistry, Japan -International Edition* 5 (2019): 2018.

16. S. Plimpton, "Fast Parallel Algorithms for Short-Range Molecular Dynamics," *Journal of Computational Physics* 117, no. 1 (1995): 1–19.

17. J. Wu, Z. Yang, X. Cai, and L. Zhang, "Dynamics of Polymer Chains Confined to a Periodic Cylinder: Molecular Dynamics Simulation vs. Lifson–Jackson Formula," *Physical Chemistry Chemical Physics* 25, no. 36 (2023): 24395–24405.

18. R. Erban, "Asymmetric Periodic Boundary Conditions for All-Atom Molecular Dynamics and Coarse-Grained Simulations of Nucleic Acids," *The Journal of Physical Chemistry B* 127, no. 38 (2023): 8257–8267.

19. H. Edelsbrunner and E. P. Mücke, "Three-Dimensional Alpha Shapes," *ACM Transactions on Graphics* 13, no. 1 (1994): 43–72.

20. T. Boontheekul, H.-J. Kong, and D. J. Mooney, "Controlling Alginate Gel Degradation Utilizing Partial Oxidation and Bimodal Molecular Weight Distribution," *Biomaterials* 26, no. 15 (2005): 2455–2465.

21. K. Y. Lee and D. J. Mooney, "Alginate: Properties and Biomedical Applications," *Progress in Polymer Science* 37, no. 1 (2012): 106–126.

22. J. M. Sonego, P. R. Santagapita, M. Perullini, and M. Jobbágy, "Ca (II) and Ce (III) Homogeneous Alginate Hydrogels from the Parent Alginic Acid Precursor: A Structural Study," *Dalton Transactions* 45, no. 24 (2016): 10050–10057.

23. J. T. Gostick, Z. A. Khan, T. G. Tranter, et al., "PoreSpy: a Python Toolkit for Quantitative Analysis of Porous Media Images," *Journal of Open Source Software* 4, no. 37 (2019): 1296.

24. B. Balakrishnan, S. Lesieur, D. Labarre, and A. Jayakrishnan, "Periodate Oxidation of Sodium Alginate in Water and in Ethanol–Water Mixture: A Comparative Study," *Carbohydrate Research* 340, no. 7 (2005): 1425–1429.

25. M. Ehsan, H. Razzaq, S. Razzaque, A. Bibi, and A. Yaqub, "Recent Advances in Sodium Alginate-Based Membranes for Dehydration of Aqueous Ethanol through Pervaporation," *Journal of Polymer Science* 60, no. 16 (2022): 2435–2453.

26. A. A. Agles and I. C. Bourg, "Structure and Dynamics of Water in Polysaccharide (Alginate) Solutions and Gels Explained by the Core–Shell Model," *Biomacromolecules* 25, no. 10 (2024): 6403–6415.

27. P. Vauchel, R. Kaas, A. Arhaliass, R. Baron, and J. Legrand, "A New Process for Extracting Alginates from Laminaria digitata: Reactive Extrusion," *Food and Bioprocess Technology*, 1, no. 3 (2008): 297–300, https://doi.org/10.1007/s11947-008-0082-x.

28. S. Saji, A. Hebden, P. Goswami, and C. Du, "A Brief Review on the Development of Alginate Extraction Process and Its Sustainability," *Sustainability*, 14, no. 9 (2022): 5181, https://doi.org/10.3390/su14095181.

Supporting Information

Additional supporting information can be found online in the Supporting Information section.

Supporting file: mame70173-sup-0001-SuppMat.docx.